ACS Photonics

Article

pubs.acs.org/journal/apchd5

Resonant Light-Induced Heating in Hybrid Cavity-Coupled 2D Transition-Metal Dichalcogenides

Hossein Taghinejad,[†] Mohammad Taghinejad,[†] Alexey Tarasov,[‡] Meng-Yen Tsai,[‡] Amir H. Hosseinnia,[†] Hesam Moradinejad,[†] Philip M. Campbell,[‡] Ali A. Eftekhar,[†] Eric M. Vogel,[‡] and Ali Adibi*[,†]

[†]School of Electrical and Computer Engineering, Georgia Institute of Technology, 778 Atlantic Drive NW, Atlanta, Georgia 30332, United States

[‡]School of Materials Science and Engineering, Georgia Institute of Technology, 771 Ferst Drive NW, Atlanta, Georgia 30332, United States

Supporting Information

ABSTRACT: Hybrid structures based on integration of two-dimensional (2D) transition-metal dichalcogenides (TMDCs) with optical resonators have recently earned significant attention. The enhanced interaction of light with 2D materials in such hybrid structures can enable devices such as efficient light-emitting diodes and lasers. However, one of the factors affecting the performance of such devices is the effect of the optically induced heat on the optoelectronic properties of the 2D materials. In this study, we systematically investigate principal roots of heat generation in hybrid cavity-coupled few-atomic-layer-thick 2D TMDC films under optical pumping. The optical resonator exploited here is a Fabry–Perot (FP) resonator, which can enhance the light–MoS_2 interaction by a significant factor of 60 at its resonance wavelength. We have combined an accurate theoretical modeling with experimental Raman spectroscopy to determine the roots of heat generation in MoS_2 films integrated with FP resonators. Our investigations reveal that the strong modulation of light absorption in the MoS_2 film, induced by excitation of an FP cavity at its resonant frequency, plays the primary role in excess heat generation in 2D materials. Furthermore, through varying the cavity length, we show that on-resonance and off-resonance excitation of the cavity results in completely different temperature profiles in the cavity-coupled MoS_2 films. Also, by changing the resonance medium of the FP cavity (SiO_2 and air), we take into account the role of the heat sinking effect of the substrate in heat generation in MoS_2 films. In this study, the temperature-dependent red-shift of the Raman spectra is employed to monitor the local temperature of the MoS_2 films. Our results show the importance of the heating effect in such hybrid structures and represent a step forward for the design of practical hybrid optical devices based on layered semiconducting 2D materials.

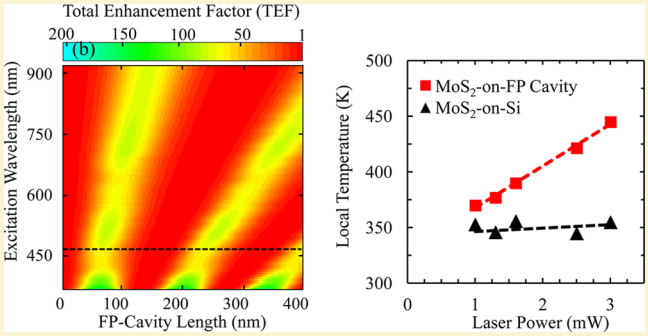

KEYWORDS: *light-induced heating, optical cavity, Fabry–Perot (FP) resonance, transition-metal dichalcogenides (TMDCs), Raman spectroscopy*

Two-dimensional (2D) layered materials such as graphene and transition-metal dichalcogenides (TMDCs) have attracted a surge of research, as they enable the development of novel optoelectronic devices at reduced dimensions (i.e., atomic-thick layers) on various substrates. However, at reduced dimensions, heating effects strongly affect optoelectronic properties of 2D materials. The significant thermoelectric and thermo-optic properties of these 2D materials have motivated extensive research recently, with a main focus being the calculation and measurement of thermal conductivity[1−4] and Seebeck coefficient.[5,6] Several device design architectures such as three-terminal field-effect transistors have also been exploited to manipulate intrinsic thermal properties of graphene[7,8] and TMDCs.[9,5] For example, Buscema et al.[9] have demonstrated 2 orders of magnitude tuning of the Seebeck coefficient of monolayers of molybdenum disulfide (MoS_2) by applying an appropriate back-gate voltage. However, most of the previous device-level studies on thermal effects have been focused on electronic devices, and attention to the photonics devices has been appreciably less. On the other hand, recent accomplishments and continuous interest in optoelectronic properties of 2D materials and, specifically, their integration with photonic and plasmonic resonators call for a systematic study of the heat generation mechanisms and the effect of heating on optoelectronic properties of such photonic and plasmonic devices. For example, integration of graphene and TMDCs with Fabry–Perot (FP) resonators,[10−12] photonic crystal cavities,[13,14] microdisk and microring resonators,[15,16] and plasmonics nanocavities[17−19] can be named. Although these works pursue different goals upon integration of 2D layered

Received: February 5, 2016
Published: March 31, 2016

ACS Publications © 2016 American Chemical Society

DOI: 10.1021/acsphotonics.6b00085
ACS Photonics 2016, 3, 700−707

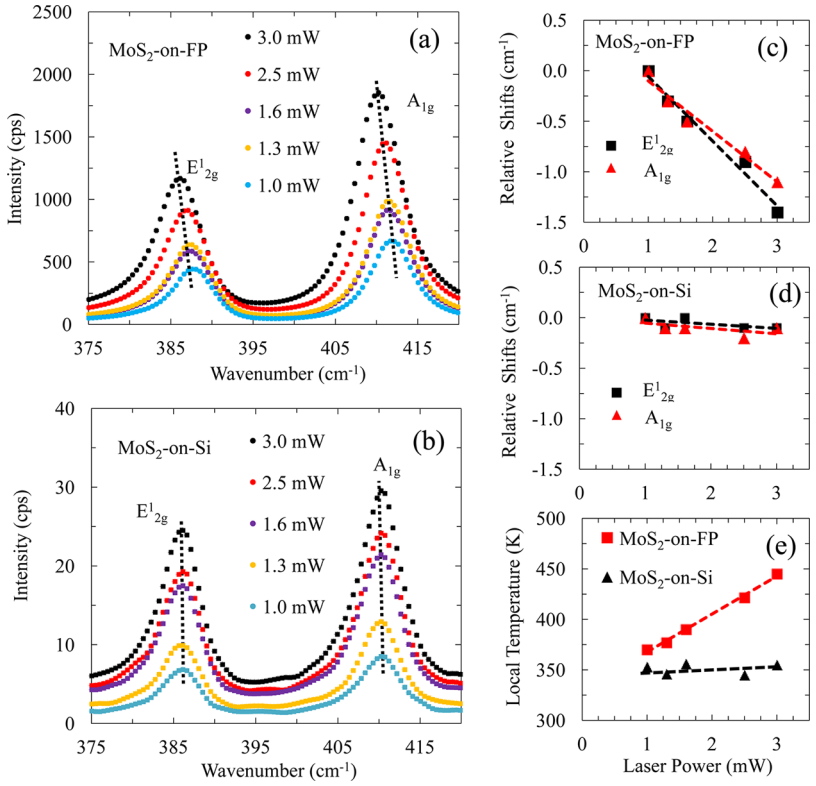

Figure 1. Effect of coupling to the FP cavity on laser-induced thermal heating of the MoS_2 films. Raman spectra are recorded at different laser powers ranging from 1 to 3 mW for (a) MoS_2-on-FP resonator (i.e., 256 nm SiO_2 on Si substrate) and (b) MoS_2-on-Si sample. The in-plane (E^1_{2g}) and out-of-plane (A_{1g}) characteristic resonances of the MoS_2 film are marked on the plots. Dashed lines are guides to the eye connecting peak positions of the E^1_{2g} and A_{1g} resonances at different laser power. Peak positions of the A_{1g} and E^1_{2g} features manifest a linear red-shift by increasing power of the excitation laser as shown in panels (c) and (d) for the MoS_2-on-FP and MoS_2-on-Si samples, respectively. (e) Local temperature of the MoS_2 film at different laser powers, calculated from the ratio of Stokes to anti-Stokes integrated intensities of the E^1_{2g} feature. The dashed lines are least-squares linear fits to the experimental data.

materials with optical resonators, they share one thing in common: strong light−matter interaction. Therefore, excess heating of the 2D material is an immediate consequence of such pronounced interactions and demands serious consideration.

In this paper, we systematically study the effect of integration of trilayer MoS_2 with an FP resonator (formed by a slab of silicon dioxide (SiO_2) grown on a silicon (Si) substrate) on laser-induced heat generation. By adjusting the wavelength of the FP resonance (through changing the cavity length, i.e., the SiO_2 thickness), we tune the strength of light−MoS_2 interaction and investigate the effect of the interaction enhancement on the amount of laser-induced heat generation. Our results reveal that the strong enhancement of light absorption in MoS_2 films enabled by integration with FP resonators plays a major role in the increase of the local temperature of the film. In this study, the red-shift of the Raman spectrum of the MoS_2 samples, measured at different excitation laser powers, is exploited to estimate the local temperature of the MoS_2 films integrated on various FP resonators. We show that, despite the relatively small quality factor of the FP resonators (because of the limited cavity length), the high refractive index contrast of MoS_2 and Si with SiO_2 results in significant enhancement of the measured Raman signal by a factor of 60.

High-quality MoS_2 films were grown by direct sulfurization of molybdenum (Mo) thin films.[20,21] Briefly, a layer of 1-nm-thick Mo film was deposited on a 260-nm-thick SiO_2 film on a Si substrate using an electron-beam evaporator, and then the sample was placed in a furnace and exposed to a controlled flow of the sulfur gas at a temperature of 1050 °C for uniform growth of MoS_2 on a large area. Following gradual cooling to 300 °C, the sample was taken out of the furnace. Using cross-sectional transmission electron microscopy (TEM, Figure S1, Supporting Information), we identified the thickness of the as-prepared films to be ∼2.1 nm, which is equivalent to the height of a trilayer MoS_2 film. The MoS_2 film was then transferred onto new substrates through a standard wet-transfer technique, which is described in the Experimental Section. Photoluminescence (PL) spectroscopy (Figure S2, Supporting Information) of the as-synthesized trilayer MoS_2 film shows that the central emission wavelengths of the A and B excitons are located at 620 nm (∼2 eV) and 670 nm (∼1.85 eV), respectively, which demonstrates 150 meV splitting of the valence band at the K-point caused by spin−orbit coupling.[22,23] These numbers are similar to those reported in theoretical modeling[22] and also for MoS_2 films synthesized by chemical vapor deposition (CVD)[24,25] and exfoliation[23,26] techniques.

Raman spectroscopy was used to monitor laser-induced heat generation in MoS_2 films integrated on FP resonators (referred to as MoS_2-on-FP in this paper). Raman spectroscopy is proven to be strongly sensitive to temperature variations.[27−30] Increasing the temperature through changing the effective binding length of vibrating molecules reduces the restoring force and softens the vibration strength.[28,29] Furthermore, at elevated temperatures, the vibration of the molecules might not be modeled as a simple harmonic oscillator. Instead, for a

DOI: 10.1021/acsphotonics.6b00085
ACS Photonics 2016, 3, 700−707

complete description, contribution of nonharmonic vibrations should also be taken into account,[27,28] which in turn contributes to the softening of the vibrations. These two effects cause a red-shift and also broadening of the Raman spectrum as the temperature increases. Figure 1a,b show the Raman spectra of the MoS_2-on-FP sample (256 nm SiO_2/Si) and on a bare Si substrate (referred to as MoS_2-on-Si in this paper), respectively, measured at several laser powers ranging from 1 to 3 mW at a pump wavelength of 488 nm. Note that the minimum laser power is chosen so that the signal-to-noise ratio of the Raman signal on the Si substrate is high enough for reliable measurements and the maximum laser power is chosen to avoid permanent damage to the MoS_2 film integrated on the FP resonators (see Figure S3, Supporting Information). In all measurements, the wavelength of the excitation laser is kept fixed at 488 nm. In these Raman spectra, the two prominent in-plane (E^1_{2g}) and out-of-plane (A_{1g}) vibrations of the MoS_2 films are observable. By fitting Lorentzian functions to the experimentally acquired spectra (Figure S4, Supporting Information), the peak positions and line widths are extracted at different laser powers. Figure 1c,d show that by increasing the excitation power the E^1_{2g} and A_{1g} Raman peaks experience linear red-shifts accompanied by line width broadening (Figure S5, Supporting Information). However, a key observation here is that the Raman spectrum of the MoS_2-on-FP sample undergoes a remarkably larger red-shift as compared to that of the MoS_2-on-Si sample. This distinction can be inferred by looking at the slope of the E^1_{2g} (A_{1g}) red-shift of the MoS_2-on-FP sample, $\chi_{E^1_{2g}} = -0.64$ cm^{-1}/mW ($\chi_{A_{1g}} = -0.47$ cm^{-1}/mW), which is about 1 order of magnitude larger than that of the MoS_2-on-Si sample (i.e., $\chi_{E^1_{2g}} = -0.05$ cm^{-1}/mW ($\chi_{A_{1g}} = -0.06$ cm^{-1}/mW)). This effect was investigated more precisely by calculating the local temperature of the MoS_2 film on the two substrates (Figure 1e) at different excitation laser powers. Here, the local temperature of the MoS_2 film is estimated using the following equation:[27]

$$\frac{I_S}{I_{AS}} = \kappa \exp\left(\frac{\hbar\omega}{K_B T}\right) \quad (1)$$

where I_S and I_{AS} are the integrated intensities of Stokes and anti-Stokes components (Figure S6, Supporting Information) of the E^1_{2g} resonance. In eq 1, $\hbar\omega$, K_B, and T are the vibration energy of the E^1_{2g} resonance, Boltzmann constant, and the local temperature of the MoS_2, respectively. Also, κ is a prefactor that accounts for absorption coefficients and scattering cross sections of the Stokes, anti-Stokes, and the incident light components in the MoS_2 film (see Supporting Information for further details). We have chosen the E^1_{2g} resonance because coupling between optically generated electrons and phonons for this vibration mode is negligible,[31] and the observed changes in the Raman spectra can safely be attributed to the heating effects only. Figure 1e indicates two important facts: (i) increasing the excitation laser power linearly increases the local temperature of the MoS_2 film. This suggests laser-induced thermal heating as the origin of the red-shift observed in the Raman spectra, which is in agreement with previous reports.[4,29,30] (ii) Excited at identical laser powers, the local temperature of the MoS_2-on-FP sample is significantly higher than that of the MoS_2-on-Si sample, which clarifies the significantly stronger red-shift of the Raman spectrum observed on the FP resonator compared to that on the Si substrate. As Figure 1e shows, the variation of the local temperature caused by varying the excitation laser power is very small for the MoS_2-on-Si sample, while it has a linear behavior with a slope of +37 K/mW for the MoS_2-on-FP sample. Indeed, excitation of the MoS_2 film on the FP resonator causes excess heating and yields a stronger red-shift. Two phenomena might contribute to this observation: (i) different thermal conductivities of the substrate materials underneath the MoS_2 films (i.e., SiO_2 versus Si) and (ii) enhanced light−MoS_2 interaction in the vicinity of the FP cavity. Since the thermal conductivity of SiO_2 is lower than that of Si, the generated heat in the MoS_2-on-FP sample dissipates more slowly and results, in part, in increasing the local temperature. On the other hand, field enhancement induced by the constructive interference of light in the FP resonator enhances light interaction with the MoS_2 film integrated on the FP resonator and builds up more heat. The strength of this effect can be more appreciated by noting that the maximum intensity of the Raman signal of the MoS_2-on-FP sample is about 45 times higher than that of the MoS_2-on-Si sample (Figure 1a,b). To identify the contribution of these two effects, by controlling the FP cavity length (i.e., thickness of the SiO_2 layer), we establish several FP resonators with different Raman enhancement strengths and repeat experiments similar to those explained in Figure 1. This allows exploring the sole role of the FP resonance in the generation of excess heat in the MoS_2-on-FP sample while the heat conductivity (i.e., heat sinking) property of the substrate in all samples are rather similar.

It is worth mentioning that the dependence of the thermal conductivity of a SiO_2 thin film on film thickness is essentially negligible if the film is thicker than approximately 150−200 nm.[32] Therefore, to avoid different heat sinking effects from the substrate, the SiO_2 layers of all the FP resonators are designed to be thick enough. Figure 2a,b represent variation of the E^1_{2g} and A_{1g} red-shifts with laser power at three FP cavity lengths of 197, 256, and 273 nm along with that of the MoS_2-on-Si sample. Our later discussions clarify the rationale behind choosing these specific thicknesses. The results shown in Figure 2 were obtained by measuring relative shifts in the peak positions of the E^1_{2g} and A_{1g} resonances at different excitation laser powers with respect to peak positions at 1 mW laser power. As is evident from Figure 2, changing the thickness of the SiO_2 slab varies the slope of the red-shift in the Raman spectrum, which is a manifestation of the increase in laser-induced heating of MoS_2. This observation is an indication of changing the strength of the laser light interaction with changing the FP resonance wavelength, which is dictated by the length of the cavity, as will be explained later. Slopes of the red-shifts for E^1_{2g} (i.e., $\chi_{E^1_{2g}}$) and A_{1g} (i.e., $\chi_{A_{1g}}$) resonances on different substrates are extracted by fitting linear trends to the experimental results in Figure 2a,b, and the quantitative values of the slopes are tabulated as shown in Figure 2c. Notice that negative signs of the slopes point to the red-shift of the resonances. Numerical values reveal that both $\chi_{E^1_{2g}}$ and $\chi_{A_{1g}}$ are considerably larger for the case where FP is excited on-resonance (i.e., cavity length of 256 nm) as compared to the off-resonance cases (i.e., cavity lengths of 197 and 273 nm). To interpret these results, we study the effect of varying SiO_2 thickness on the interference of light inside the FP cavity and its effect on modulation of light interaction with the MoS_2 film through a numerical model based on successive reflections of light from the boundaries of the SiO_2 slab (as shown in Figure 3a), which is formulated by Li et al.[33] Details of the calculations are available in the Supporting Information. As a figure of merit,

DOI: 10.1021/acsphotonics.6b00085
ACS Photonics 2016, 3, 700−707

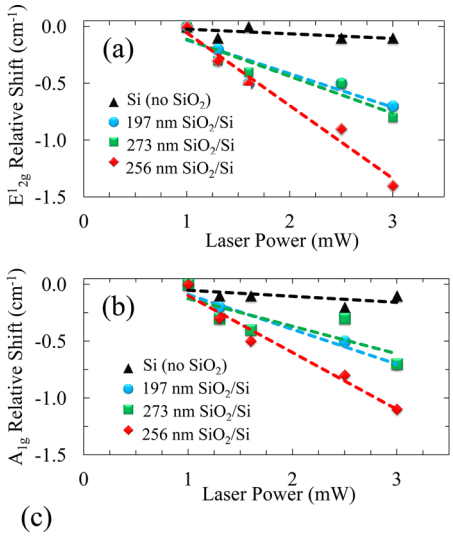

Substrate	$\chi_{E^1_{2g}}$ (cm^{-1}/mW)	$\chi_{A_{1g}}$ (cm^{-1}/mW)
Si (no SiO_2)	-0.05	-0.06
197 nm SiO_2/Si	-0.27	-0.26
273 nm SiO_2/Si	-0.31	-0.26
256 nm SiO_2/Si	-0.64	-0.47

Figure 2. Variation of the red-shift experienced by (a) E^1_{2g} and (b) A_{1g} vibrations of the trilayer MoS_2-on-FP sample through changing cavity length (i.e., thickness of the SiO_2 slab). For the sake of comparison, red-shifts of E^1_{2g} and A_{1g} resonances on the Si substrate (no SiO_2) at different laser powers are also represented. Symbols are experimental results, and dashed lines are linear fits. (c) Quantitative values for the slopes of the MoS_2 Raman red-shifts on different substrates are tabulated for E^1_{2g} (i.e., $\chi_{E^1_{2g}}$) and A_{1g} (i.e., $\chi_{A_{1g}}$) resonances. Negative signs of the slopes are an indication of the red-shift.

we define the total enhancement factor (TEF) as the ratio of the maximum intensity of the E^1_{2g} Raman peak of the MoS_2-on-FP samples ($I_{max,\ FP}$) to that of the MoS_2-on-Si sample ($I_{max,\ Si}$), that is, TEF = $I_{max,FP}/I_{max,Si}$. The map of Figure 3b illustrates the results of this modeling for trilayer MoS_2 films integrated on FP resonators with various SiO_2 thicknesses, while the excitation laser wavelength varies between 380 and 900 nm. In this map, at a fixed SiO_2 thickness, the wavelength-dependent enhancement profile illustrates irregularities that originate from the combined effect of the FP interference and the wavelength-dependent refractive index of the MoS_2 film[33−35] (Figure S8, Supporting Information). At a fixed excitation wavelength, however, the enhancement spectrum periodically depends on the thickness of the SiO_2 layer. Figure 3c shows the variation of the TEF with the SiO_2 thickness at the excitation wavelength of λ = 488 nm (used in our experiments) associated with the dashed line overlaid on the 2D map of Figure 3b. Figure 3c suggests that the maximum enhancement can be reached, to a first-order approximation, when the SiO_2 thickness is equal to the odd multiples ($2l + 1$) of one-quarter of the wavelength in the resonance medium ($\frac{\lambda}{4n}$); that is

$$d_{l,\max} = (2l + 1)\frac{\lambda}{4n} \quad (2)$$

where n and l are the refractive index of SiO_2 (∼1.46) and an integer number (mode index), respectively. However, the fairly large imaginary part of the refractive index of MoS_2 at λ = 488 nm (∼1.65) gives rise to a reflection phase addition at the MoS_2/SiO_2 interface, which is not considered in eq 2. Thereby, a thinner SiO_2 (less than what eq 2 predicts) meets the condition for the maximum enhancement of the E^1_{2g} Raman peak. For example, eq 2 predicts $d_{l=0,max}$ = 83 nm, while the results of more complete modeling determine an optimal thickness of 67 nm. Nevertheless, eq 2 clearly elucidates the periodic dependence of the TEF on the SiO_2 thickness with a period of $\frac{\lambda}{2n}$ = 167 nm, very close to 165 nm that the results of modeling (Figure 3) predict. To verify accuracy of our modeling, Figure 3c represents the experimentally measured TEFs (square symbols) for the three MoS_2-on-FP samples (used in the Raman measurements of Figure 2). Good agreement between the simulation and the experimental results for the three samples is evident from Figure 3c. Notice that the 5−7 cm^{-1} line width of the E^1_{2g} Raman resonance is equivalent to less than a 1 nm spectral width. Therefore, we can safely assume that the entire E^1_{2g} resonance spectrum gains an identical enhancement and variation of the TEF over the Raman line width is negligible. Detailed discussion regarding the effect of the MoS_2 thickness on the TEF is presented in the Supporting Information.

Comparing the TEF of the E^1_{2g} peak intensity of MoS_2 on different FP resonators (Figure 3c) with the slope of the red-shift of the E^1_{2g} resonance (as an indication of the local temperature) on corresponding substrates (Figure 2a) provides insightful information. FP cavities with 197, 256, and 273 nm SiO_2 thicknesses provide TEFs of 5.6, 45.6, and 26.9 for the E^1_{2g} resonance, respectively. The corresponding $\chi_{E^1_{2g}}$'s on these substrates are −0.27, −0.64, and −0.32 cm^{-1}/mW, respectively. In other words, the higher the TEF, the larger the slope of the red-shift of the Raman spectra. This confirms the principal role of the enhanced interaction of light with MoS_2 on excess heat generation. However, although the TEF on the FP resonator with 256 nm SiO_2 is more than 8 times larger than that on the FP resonator with 197 nm SiO_2, the slope of the red-shift on the 256 nm SiO_2 substrate is only 2 times larger than that of the resonator with 197 nm SiO_2 thickness. More interestingly, the FP cavity with the SiO_2 thickness of 273 nm provides a TEF of approximately 5 times larger than that on the FP cavity with 197 nm SiO_2 thickness, while the slope of the red-shift on the 273 nm SiO_2 resonator is just slightly larger than that of the 197 nm SiO_2 resonator. This inconsistency between the TEFs and the red-shifts of the E^1_{2g} resonance can be resolved by considering details of the enhancement mechanism. Improvement of the Raman intensity of the MoS_2-on-FP samples has two roots: (1) enhancement of the MoS_2 excitation (equivalently, light absorption) and (2) enhancement of the Raman scattering (emission) from the MoS_2 film (see Figure 3a). A combination of the improved excitation and emission contributes to the enhancement of the Raman signal of the MoS_2-on-FP sample and determines the TEF. However, the heat generation is primarily entangled with the enhancement of the light absorption. Therefore, we need to introduce two separate enhancement factors: absorption enhancement factor (AEF) and scattering enhancement factor (SEF). In Figure 3d, we present the dependence of these two factors on the thickness of the SiO_2 cavity at an excitation wavelength of 488 nm (see Supporting Information for details). In these

DOI: 10.1021/acsphotonics.6b00085
ACS Photonics 2016, 3, 700−707

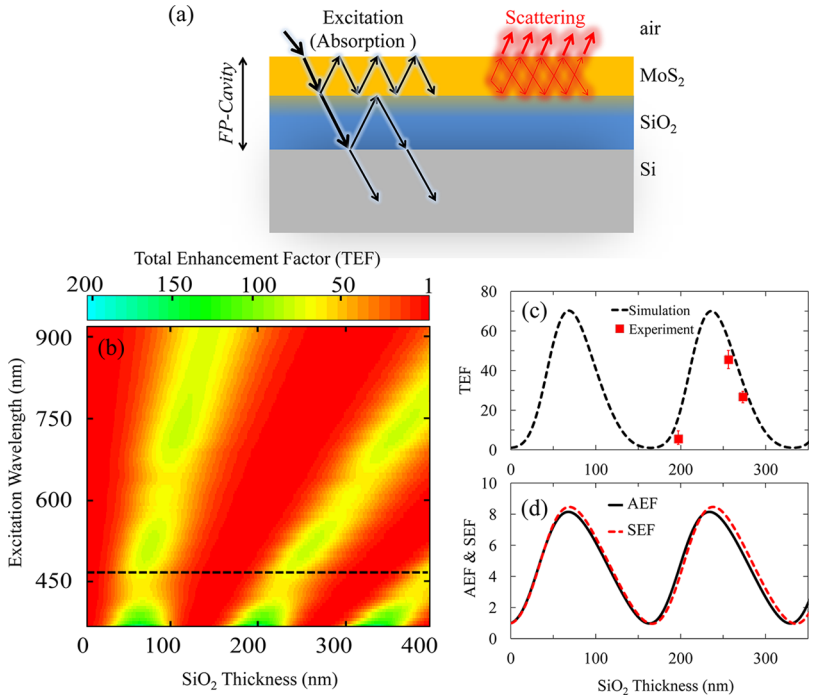

Figure 3. Enhanced light–MoS_2 interaction induced by constructive interferences on the FP cavity (studied for E^1_{2g} Raman resonance). (a) Schematic illustration of the cavity structure in which ray trace is used to show the propagation of light beams inside the cavity. (b) Simulation results representing the enhancement of the Raman signal of the MoS_2-on-FP sample as a function of the SiO_2 thickness (cavity length) and the wavelength of the excitation laser. The color bar represents the expected enhancement factor induced by the FP resonance. (c) Enhancement spectra at 488 nm excitation wavelength (used in our measurements) for the trilayer MoS_2 film on the SiO_2 substrate (corresponding to the dashed line overlaid on the map of part "b"). Squares represent the experimental results. (d) Separate contribution of the improved light absorption (i.e., AEF) and light scattering (i.e., SEF), as represented in the schematic illustration of part "a", to the total enhancement of the E^1_{2g} Raman signal (i.e., TEF) at the 488 nm excitation wavelength as a function of the SiO_2 thickness.

calculations, AEF and SEF are computed by dividing, respectively, the absorption and scattering components of the Raman signal of the MoS_2-on-FP samples by the corresponding components of the MoS_2-on-Si sample. Figure 3d shows that the AEF and SEF have similar profiles with maximum enhancement factors of approximately 8. This general resemblance is due to the small energy exchange upon E^1_{2g} Raman scattering, which results in a small wavelength shift between incoming and scattered light and, thus, leads to similar FP cavity response for the excitation and scattering signals. However, since the wavelength of the scattered light is slightly longer than that of the incoming light (Stokes shift), based on eq 2, the maximum enhancement for the scattering profile occurs at a slightly thicker SiO_2 layer than that for the absorption profile in Figure 3d. Further minute differences between the absorption and scattering spectra, in Figure 3d, can be related to the wavelength-dependent reflection of light (for the incoming and scattered light) at the MoS_2–SiO_2 boundary caused by the dependence of the refractive index of MoS_2 on the wavelength.

Figure 3d shows that for MoS_2-on-FP samples with SiO_2 thicknesses of 197, 256, and 273 nm, light absorption by MoS_2 gains enhancement factors of AEF = 3.9, 7.3, and 4.3, respectively. Comparing these values with the slope of the red-shift on the corresponding substrates (Figure 2c) reveals that the trend of the red-shift agrees well with the trend of the absorption enhancement. For example, the AEF for the FP resonator with a 256 nm SiO_2 layer is approximately twice that for the resonator with 197 nm SiO_2, which is consistent with the slope of the E^1_{2g} red-shifts on these two samples. Likewise, a similar absorption enhancement on resonators with 197 and 273 nm SiO_2 layers is consistent with rather identical slopes for the E^1_{2g} red-shifts of the Raman resonances on these substrates. These observations suggest that modulation of the light absorption (not the total enhancement) is the underlying mechanism for the excess heat generation in MoS_2-on-FP structures, which manifests itself in the amount of the red-shift observed in the Raman spectra. Therefore, the in-resonance excitation of the FP cavity (as in a sample with a 256 nm SiO_2 layer) increases the MoS_2 temperature significantly more than the off-resonance excitation (as in samples with 197 and 273 nm SiO_2 layers).

Another phenomenon that affects heating in the integrated 2D materials on resonators is the heat conductivity of the substrate (or the substrate heat sinking effect). To study this effect, we etch an array of holes with diameters of 4–5 μm into the 256-nm-thick SiO_2 on the Si substrate and then suspend the trilayer MoS_2 film over it (Figure 4a and Figure S10a, Supporting Information) to establish two types of FP resonators that are spatially adjacent: one resonator has a 256 nm air gap as the resonance medium (i.e., the suspended MoS_2 region over the holes) and the other one has a 256 nm SiO_2 as the resonance medium (i.e., the supported MoS_2 regions outside the holes). In these two types of resonators, different thermal conductivities of the air and SiO_2 allow investigating the strength of the heat sinking effect of the substrate on heat generation in a MoS_2 film. We map the Raman spectrum of the MoS_2 across a line passing over one of the holes, at a fixed laser power of 3 mW, and record the Stokes and anti-Stokes spectra. Figure 4b illustrates the map of Stokes Raman spectra at

DOI: 10.1021/acsphotonics.6b00085
ACS Photonics 2016, 3, 700–707

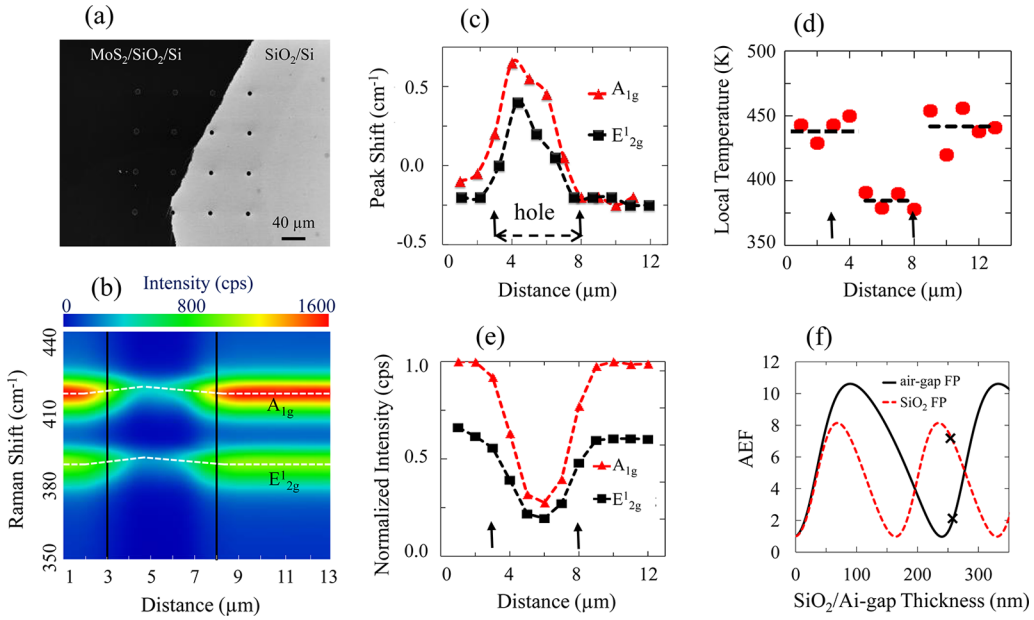

Figure 4. (a) SEM image of the trilayer MoS_2 film suspended over an array of holes etched into a 256-nm-thick SiO_2 layer on a Si substrate. The darker region on the left-hand side is covered with MoS_2. (b) Raman mapping across a line passing over a hole in (a), where MoS_2 is suspended. Horizontal dashed lines are guides to the eyes showing peak positions of the A_{1g} and E^1_{2g} resonances. Vertical lines depict edges of the hole in the line scan. (c) Relative change of the A_{1g} and E^1_{2g} peak positions across the scanned line compared to a reference point outside the hole. By moving from outside toward the center of the hole, both resonances manifest a symmetric blue-shift that reaches their maxima at the center of the hole. Dashed lines are guides to the eyes. The arrows show the extent of the hole. (d) Spatial temperature profile across the scanned line where three regions are distinguishable: suspended MoS_2 at the middle (i.e., over the hole) and SiO_2-supported MoS_2 at the left and right regions (outside the hole). Dashed lines show the average temperature at each region. The arrows show the extent of the hole. (e) Normalized intensity profiles of the A_{1g} and E^1_{2g} across the scanned line. By moving from outside toward the center of the hole, the intensity of both features is symmetrically reduced and reaches the minimum value at the center of the hole. Dashed lines are guides to the eyes. The arrows show the extent of the hole. (f) Comparing enhancement of light absorption (i.e., AEF) in the MoS_2 film integrated on SiO_2 (dashed line) and air-gap (solid line) FP cavities. The crosses mark the values for the specific cavity length of 256 nm, which is used in our experiment.

different positions, where the dashed lines mark the peak positions of the E^1_{2g} and A_{1g} vibrations and the solid vertical lines outline edges of the hole, where MoS_2 is suspended. The Raman map of the anti-Stokes spectrum is presented in Figure S11 of the Supporting Information. In order to monitor the evolution of the E^1_{2g} and A_{1g} resonances, we pick vibration frequencies of a point outside the hole as the reference to measure the relative shifts of the E^1_{2g} and A_{1g} resonances along the scanned line (Figure 4c). The results show that by moving from a point outside the hole toward the center of the hole both vibrations experience symmetric blue-shifts and reach their maxima at the center of the hole. Also, in Figure 4d, we have estimated a spatial temperature profile (based on eq 1) along the scanned line where local temperature of the MoS_2 film drops from an average value of 432 K over the SiO_2-supported regions to 380 K over the suspended regions. Therefore, the blue-shifts observed in Figure 4c are due to the lower local temperature of the suspended MoS_2 compared to that of the SiO_2-supported regions. Figure 4e depicts the normalized Raman scattering intensities corresponding to the E^1_{2g} and A_{1g} vibrations, where both manifest a symmetric drop moving toward the center of the hole, indicating weaker light–matter interaction in the suspended MoS_2 regions compared to that of the SiO_2-supported regions. In fact, despite the better thermal conductivity of SiO_2 compared to the air, stronger light–MoS_2 interaction in SiO_2-supported regions elevates the MoS_2 temperature outside the holes and creates the temperature profile of Figure 4d and (as a direct result) the blue-shift profile of Figure 4c. To verify this claim, in Figure 4f, we have compared AEFs of FP resonators having either an air gap or SiO_2 as the resonance medium through the same method used above (refer to Figure S10 in the Supporting Information for the complete wavelength-dependent map showing the TEF of the Raman signal at different cavity lengths for air-gap FP cavities). In Figure 4f, owing to the larger refractive index of the SiO_2, the maximum absorption enhancement can be reached at a shorter cavity length (compared to the air-gap FP resonator), as predicted by eq 2. Also, a maximum achievable AEF on the air-gap resonator (~11) is larger than that over the SiO_2 resonator (~8). This effect can be explained on the basis of the refractive index contrast at the upper (i.e., MoS_2–SiO_2/air) and lower (Si–SiO_2/air) boundaries of the two types of FP cavities. Higher refractive index contrast provides larger reflection coefficients at the two boundaries and increases the quality factor of the cavity. Therefore, knowing that the refractive index contrasts at both upper and lower boundaries are larger for the air-gap cavity compared to the SiO_2 cavity, we expect a higher quality factor for the former resonator. Thus, potentially, the air-gap resonator enables stronger light–MoS_2 interaction than the resonators having SiO_2 as the resonance medium. However, for the specific cavity length of 256 nm (used in the analysis of Figure 4), the AEFs are 7.4 and 1.4 over the SiO_2-supported and air-gap FP resonators, respectively (as marked by two crosses in Figure 4f). This is primarily due to the existence of an FP cavity mode in the SiO_2 resonator at the excitation wavelength of 488 nm and lack of such mode in the air-gap cavity. In other words, while excitation at 488 nm wavelength is on-resonance for a SiO_2 FP cavity, it is an off-

DOI: 10.1021/acsphotonics.6b00085
ACS Photonics 2016, 3, 700–707

resonance excitation for the air-gap FP cavity. Therefore, illuminated at identical laser powers, a greater portion of light gets absorbed by MoS_2 films integrated over the SiO_2 FP resonator compared to that over the air-gap resonator, which generates the temperature profile of Figure 4d. Results of Figure 4 demonstrate that the effect of absorption modulation can completely overwhelm the heat sinking effect of the substrate material and governs the heat generation upon coupling of the 2D materials to the optical cavities. It can also be inferred that by selecting the proper cavity length for the SiO_2 and air-gap resonators a large range of performance variations can be achieved.

The results of this paper clearly show the importance of the thermal effects in changing the optical properties of the 2D materials integrated with photonic resonators. These thermal effects are inherent in the optical characterization of resonance-enhanced phenomena in hybrid integration of 2D materials with photonic (or plasmonic) structures. Thus, extreme care must be given to the interpretation of the experimental results in such studies by decoupling the light-induced thermal effects (that usually result in changing the temperature distribution over the 2D material) from the other (desired) effects (e.g., effects of strain or composition change on optoelectronic properties of 2D materials).

In addition to its importance in proper interpretation of the experimental results, the outcomes of this paper can be useful from a practical perspective, especially for energy-harvesting applications. As an example, the spatial modulation of the light absorption in MoS_2 through substrate engineering can be exploited for artificial generation of a temperature gradient (as in Figure 4d). Knowing that MoS_2 has a large Seebeck coefficient (up to 30 mV/K[5]), this temperature gradient can be converted into an electric signal (e.g., voltage) by application of two electrodes (e.g., indium−tin-oxide) at cold and hot regions. Indeed, through a photothermoelectric conversion chain, light generates a temperature gradient (e.g., 50 K in Figure 4d) that can be converted into a voltage difference through the Seebeck effect (e.g., between the hole center and the surrounding region in Figure 4a). This effect can be optimized by engineering the shape and distribution of the holes in Figure 4a. A separate study is currently under way to explore the practical prospects of this idea.

In conclusion, we investigated here the effect of enhanced light−matter interaction on laser-induced heating of 2D materials integrated with photonic resonators. The heating mechanism in such structures was studied using a combination of Raman spectroscopy and theoretical modeling. We showed that the strong modulation of the light absorption of MoS_2 by the optical resonator results in a considerable increase in the local temperature of the MoS_2. Also, exploiting an air-gap FP cavity, we demonstrated that the strength of the light−matter interaction plays a much more important role than the changes in the substrate heat sinking effect. We believe that the results of our work are important for a correct and comprehensive interpretation of the optical characterization of 2D materials integrated with optical resonators as well as introduction of new platforms for practical applications such as energy harvesting.

EXPERIMENTAL SECTION

MoS_2 Transfer. To ensure that the MoS_2 films possess similar optical quality in all samples, a large-area MoS_2 film was grown on a large SiO_2/Si wafer, and then the wafer was cleaved into several smaller pieces to be transferred onto the FP resonators of different cavity lengths. The size of the parent wafer was chosen such that spatial nonuniformity is minimized. Then, a thick layer of poly(methyl methacrylate) (PMMA) was spin coated on the surface of each sample to serve as a support for the MoS_2 film during the transfer process. Afterward, the sample was dipped into buffered oxide etchant (overnight) to etch the 260 nm SiO_2 layer underneath the MoS_2 film and release it from the substrate and float it over the liquid. The floating MoS_2/PMMA was then fished with the target substrate. Finally, the PMMA was removed from the MoS_2 surface by immersing the sample into acetone for 2 h followed by rinsing it with deionized water and drying with a flow of nitrogen gas.

Raman Measurements. Raman spectra were collected in a dispersive micro-Raman spectrometer (Thermo Nicolet Almega XR) in a back-scattering configuration with an excitation wavelength of 488 nm (Ar laser). Several Raman spectra were collected at the laser powers of 1, 1.3, 1.6, 2.5, and 3 mW. A notch filter was centered at the laser line to reject the Rayleigh scattering. Using a 100× objective lens (NA = 0.65), the laser beam was focused to a spot size of 0.5 μm on the sample, and the Raman scattered light was collected with the same objective lens.

ASSOCIATED CONTENT

Supporting Information

The Supporting Information is available free of charge on the ACS Publications website at DOI: 10.1021/acsphotonics.6b00085.

Photoluminescence spectra of trilayer MoS_2, SEM images of damaged MoS_2 at high laser power, Lorentzian curve fitting to Raman spectra, laser power-dependent line width broadening of Raman spectra, anti-Stokes Raman spectra, calculation of κ, modeling of TEF, AEF, and SEF, wavelength-dependent refractive index of MoS_2, the effect of the MoS_2 thickness on TEF, and TEF for air-gap FP resonator (PDF)

AUTHOR INFORMATION

Corresponding Author

*E-mail: ali.adibi@ece.gatech.edu.

Notes

The authors declare no competing financial interest.

ACKNOWLEDGMENTS

This work was primarily funded by the Air Force Office of Scientific Research (AFOSR) under Grant No. FA9550-13-1-0032 (G. Pomrenke). The material development part is also supported by the Swiss National Science Foundation (SNF) under Grant Nos. P2BSP2_148636 and P300P2_158502 (to A.T.); the National Science Foundation (through CBET-1264705); the Center for Low Energy Systems Technology, one of six centers supported by the STARnet phase of the Focus Center Research Program, a Semiconductor Research Corporation program sponsored by MARCO and DARPA; and the Georgia Tech Research Institute Robert G. Shackelford Fellowship (to P.M.C.).

REFERENCES

(1) Cai, Y.; Lan, J.; Zhang, G.; Zhang, Y. W. Lattice Vibrational Modes and Phonon Thermal Conductivity of Monolayer MoS_2. *Phys. Rev. B: Condens. Matter Mater. Phys.* **2014**, *89*, 035438.

DOI: 10.1021/acsphotonics.6b00085
ACS Photonics 2016, 3, 700−707

(2) Cai, W.; Moore, A. L.; Zhu, Y.; Li, X.; Chen, S.; Shi, L.; Ruoff, R. S. Thermal Transport in Suspended and Supported Monolayer Graphene Gown by Chemical Vapor Deposition. *Nano Lett.* **2010**, *10*, 1645−1651.
(3) Balandin, A. A.; Ghosh, S.; Bao, W.; Calizo, I.; Teweldebrhan, D.; Miao, F.; Lau, C. N. Superior Thermal Conductivity of Single-Layer Graphene. *Nano Lett.* **2008**, *8*, 902−907.
(4) Raman, T.; Yan, R.; Simpson, J. R.; Bertolazzi, S.; Brivio, J.; Watson, M.; Wu, X.; Kis, A.; Luo, T.; Walker, A. R. H.; Xing, H. G. Thermal Conductivity of Monolayer Molybdenum Disulfide Obtained from Spectroscopy. *ACS Nano* **2014**, *8*, 986−993.
(5) Wu, J.; Schmidt, H.; Amara, K. K.; Xu, X.; Eda, G.; Ozyilmaz, B. Large Thermoelectricity via Variable Range Hopping in CVD Grown Single-layer MoS_2. *Nano Lett.* **2014**, *14*, 2730−2734.
(6) Li, X.; Yin, J.; Zhou, J.; Wang, Q.; Guo, W. Exceptional High Seebeck Coefficient and Gas-Flow-Induced Voltage in Multilayer Graphene. *Appl. Phys. Lett.* **2012**, *100*, 183108.
(7) Freitag, M.; Low, T.; Avouris, P. Increased Responsivity of Suspended Graphene Photodetectors. *Nano Lett.* **2013**, *13*, 1644−1648.
(8) Herring, P. K.; Hsu, A. L.; Gabor, N. M.; Shin, Y. C.; Kong, J.; Palacios, T.; Jarillo-Herrero, P. Photoresponse of an Electrically Tunable Ambipolar Graphene Infrared Thermocouple. *Nano Lett.* **2014**, *14*, 901−907.
(9) Buscema, M.; Barkelid, M.; Zwiller, V.; Van Der Zant, H. S. J.; Steele, G.; Castellanos-gomez, A. Large and Tunable Photothermoelectric Effect in Single-Layer MoS_2. *Nano Lett.* **2013**, *13*, 358−363.
(10) Schwarz, S.; Dufferwiel, S.; Walker, P. M.; Withers, F.; Trichet, A. A. P.; Sich, M.; Li, F.; Chekhovich, E. A.; Borisenko, D. N.; Kolesnikov, N. N.; Novoselov, K. S.; Skolnick, M. S.; Smith, J. M.; Krizhanovskii, D. N.; Tartakovskii, A. I. Two-Dimensional Metal-Chalcogenide Films in Tunable Optical Microcavities. *Nano Lett.* **2014**, *14*, 7003−7008.
(11) Liu, X.; Galfsky, T.; Sun, Z.; Xia, F.; Lin, E. Strong Light-Matter Coupling in Two-Dimensional Atomic Crystals. *Nat. Photonics* **2014**, *9*, 30−34.
(12) Thareja, V.; Kang, J.; Yuan, H.; Milaninia, K.; Hwang, H. Y.; Cui, Y.; Kik, P. G.; Brongersma, M. Electrically Tunable Coherent Optical Absorption in Graphene with Ion Gel. *Nano Lett.* **2015**, *15*, 1570−1576.
(13) Wu, S.; Buckley, S.; Schaibley, J. R.; Feng, L.; Yan, J.; Mandrus, D. G.; Hatami, F.; Yao, W.; Vučković, J.; Majumdar, A.; Xu, X. Monolayer Semiconductor Nanocavity Lasers with Ultralow Thresholds. *Nature* **2015**, *520*, 69−73.
(14) Wu, S.; Buckley, S.; Jones, A. M.; Ross, J. S.; Ghimire, N. J.; Yan, J.; Mandrus, D. G.; Yao, W.; Hatami, F.; Vučković, J.; Majumdar, A.; Xu, X. Control of Two-Dimensional Excitonic Light Emission via Photonic Crystal. *2D Mater.* **2014**, *1*, 011001.
(15) Qiu, C.; Gao, W.; Vajtai, R.; Ajayan, P. M.; Kono, J.; Xu, Q. Efficient Modulation of 1.55 μm Radiation with Gated Graphene on a Silicon Microring Resonator. *Nano Lett.* **2014**, *14*, 6811−6815.
(16) Reed, J. C.; Zhu, A. Y.; Zhu, H.; Yi, F.; Cubukcu, E. Wavelength Tunable Microdisk Cavity Light Source with a Chemically Enhanced MoS_2 Emitter. *Nano Lett.* **2015**, *15*, 1967−1971.
(17) Butun, S.; Tongay, S.; Aydin, K. Enhanced Light Emission from Large-Area Monolayer MoS_2 Using Plasmonic Nanodisc Arrays. *Nano Lett.* **2015**, *15*, 2700−2704.
(18) Lee, B.; Park, J.; Han, G. H.; Ee, H. S.; Naylor, C. H.; Liu, W.; Johnson, A. T. C.; Agarwal, R. Fano Resonance and Spectrally Modified Photoluminescence Enhancement in Monolayer MoS_2 Integrated with Plasmonic Nanoantenna Array. *Nano Lett.* **2015**, *15*, 3646−3653.
(19) Najmaei, S.; Mlayah, A.; Arbouet, A.; Girard, C.; Leotin, J.; Lou, J. Plasmonic Pumping of Excitonic Photoluminescence in Hybrid. *ACS Nano* **2014**, *8*, 12682−12689.
(20) Tarasov, A.; Campbell, P. M.; Tsai, M. Y.; Hesabi, Z. R.; Feirer, J.; Graham, S.; Ready, W. J.; Vogel, E. M. Highly Uniform Trilayer Molybdenum Disulfide for Wafer-Scale Device Fabrication. *Adv. Funct. Mater.* **2014**, *24*, 6389−6400.
(21) Tarasov, A.; Zhang, S.; Tsai, M. Y.; Campbell, P. M.; Graham, S.; Barlow, S.; Marder, S. R.; Vogel, E. M. Controlled Doping of Large-Area Trilayer MoS_2 with Molecular Reductants and Oxidants. *Adv. Mater.* **2015**, *27*, 1175−1181.
(22) Cheiwchanchamnangij, T.; Lambrecht, W. R. L. Quasiparticle band structure calculation of monolayer, bilayer, and bulk MoS_2. *Phys. Rev. B: Condens. Matter Mater. Phys.* **2012**, *89*, 205302.
(23) Mak, K. F.; Lee, C.; Hone, J.; Shan, J.; Heinz, T. F. Atomically Thin MoS_2: A New Direct-Gap Semiconductor. *Phys. Rev. Lett.* **2010**, *105*, 136805.
(24) Lee, Y. H.; Zhang, X. Q.; Zhang, W.; Chang, M. T.; Lin, C. T.; Chang, K. D.; Yu, Y. C.; Wang, J. T. W.; Chang, C. S.; Li, L. J.; Lin, T. W. Synthesis of Large-Area MoS_2 Atomic Layers with Chemical Vapor Deposition. *Adv. Mater.* **2012**, *24*, 2320−2325.
(25) Jeon, J.; Jang, S. K.; Jeon, S. M.; Yoo, G.; Jang, Y. H.; Park, J. H.; Lee, S. Layer-controlled CVD growth of large-area two-dimensional MoS_2 films. *Nanoscale* **2015**, *7*, 1688−1695.
(26) Eda, G.; Yamaguchi, H.; Voiry, D.; Fujita, T.; Chen, M.; Chhowalla, M. Photoluminescence from Chemically Exfoliated MoS_2. *Nano Lett.* **2011**, *11*, 5111−5116.
(27) Balkanski, E. H. M.; Wallis, R. F. Anharmonic Effects in Light Scattering Due to Optical Phonons in Silicon. *Phys. Rev. B: Condens. Matter Mater. Phys.* **1983**, *28*, 1928−1934.
(28) Menendez, J.; Cardona, M. Temperature Dependence of the First-Order Raman Scattering by Phonon in Si, Ge, and a-Sn: Anharmonic Effects. *Phys. Rev. B: Condens. Matter Mater. Phys.* **1984**, *29*, 2051−2059.
(29) Sahoo, S.; Gaur, A. P. S.; Ahmadi, M.; Katiyar, R. S. Temperature-Dependent Raman Studies and Thermal Conductivity of Few-Layer MoS_2. *J. Phys. Chem. C* **2013**, *117*, 9042−9047.
(30) Lanzillo, N. A.; Birdwell, A. G.; Amani, M.; Crowne, F. J.; Shah, P. B.; Najmaei, S.; Liu, Z.; Ajayan, P. M.; Lou, J.; Dubey, M.; Nayak, S. K.; O'Regan, T. P. Temperature-Dependent Phonon Shifts in Monolayer MoS_2. *Appl. Phys. Lett.* **2013**, *103*, 093102.
(31) Chakraborty, B.; Bera, A.; Muthu, D. V. S.; Bhowmick, S.; Waghmare, U. V.; Sood, A. K. Symmetry-Dependent Phonon Renormalization in Monolayer MoS_2 Transistor. *Phys. Rev. B: Condens. Matter Mater. Phys.* **2012**, *85*, 2−5.
(32) Chien, H. C.; Yao, D. J.; Huang, M. J.; Chang, T. Y. Thermal Conductivity Measurement and Interface Thermal Resistance Estimation Using SiO_2 Thin Film. *Rev. Sci. Instrum.* **2008**, *79*, 054902.
(33) Li, S. L.; Miyazaki, H.; Song, H.; Kuramochi, H.; Nakaharai, S.; Tsukagoshi, K. Quantitative Raman Spectrum and Reliable Thickness Identification for Atomic Layers on Insulating Substrates. *ACS Nano* **2012**, *6*, 7381−7388.
(34) Lien, D. H.; Kang, J. S.; Amani, M.; Chen, K.; Tosun, M.; Wang, H. P.; Roy, T.; Eggleston, M. S.; Wu, M. C.; Dubey, M.; Lee, S. C.; He, J. H.; Javey, A. Engineering Light Outcoupling in 2D Materials. *Nano Lett.* **2015**, *15*, 1356−1361.
(35) Buscema, M.; Steele, G. A.; van der Zant, H. S. J.; Castellanos-Gomez, A. The effect of the substrate on the Raman and photoluminescence emission of single-layer MoS_2. *Nano Res.* **2014**, *7*, 561−571.

DOI: 10.1021/acsphotonics.6b00085
ACS Photonics 2016, 3, 700−707